Spherical Nanoindentation Stress-Strain Analysis of Ion-Irradiated Tungsten

Siddhartha Pathak, Jordan S. Weaver, Cheng Sun, Yongqiang Wang, Surya R. Kalidindi and Nathan A. Mara

Abstract This paper discusses applications of spherical nanoindentation stress-strain curves in characterizing the local mechanical behavior of materials with modified surfaces. Using ion-irradiated tungsten as a specific example, this paper demonstrates that a simple variation of the indenter size (radius) can identify the depth of the radiation-induced-damage zone, as well as quantify the behavior of the damaged zone itself. Using corresponding local structure information from electron backscatter diffraction (EBSD) and transmission electron microscopy (TEM) we look at (a) the elastic response, elasto-plastic transition, and onset of plasticity in ion-irradiated tungsten, zirconium and 304 stainless steel under indentation, and compare their relative mechanical behavior to the unirradiated state, (b) correlating these changes to the different grain orientations as a function of (c) irradiation from different sources (such as He, W, and He+W for tungsten samples).

Keywords Nanoindentation stress-strain · Radiation damage gradient · Stress saturation · Electron back-scattered diffraction · Transmission electron microscopy

S. Pathak (✉)
Chemical and Materials Engineering, University of Nevada,
1664 N Virginia St., Mail Stop 0388, Reno, NV 89557, USA
e-mail: spathak@unr.edu; siddharthapathak@gmail.com

J.S. Weaver · N.A. Mara
Los Alamos National Laboratory, Center for Integrated Nanotechnologies,
Los Alamos, NM 87545, USA

C. Sun · Y. Wang · N.A. Mara
Materials Science and Technology Division,
Los Alamos National Laboratory, Los Alamos, NM 87545, USA

S.R. Kalidindi
George W. Woodruff School of Mechanical Engineering,
Georgia Institute of Technology, Atlanta, GA 30332, USA

Present Address:
C. Sun
Idaho National Laboratory, Idaho Falls 83415, USA

© The Minerals, Metals & Materials Society 2019

J.H. Jackson et al. (eds.), *Proceedings of the 18th International Conference on Environmental Degradation of Materials in Nuclear Power Systems – Water Reactors*,
The Minerals, Metals & Materials Series, https://doi.org/10.1007/978-3-030-04639-2_40

Introduction

Ion beam irradiation is a novel technique to impart large amounts of irradiation damage (several dpa or more without activating the entire volume of material) in relatively short time spans of hours or days that would require months or years to achieve in reactor conditions [1–4]. Ion beam irradiation facilities can currently irradiate materials to high dpas at prototypic reactor temperatures to emulate radiation effects in different reactor conditions. However, the volume of irradiated material is limited by the beam energy to depths of fractions of a micron to several microns, making the investigation of bulk mechanical properties unachievable. The lack of validated methods to characterize the changes in the local anisotropic elastic-plastic properties of the microscale constituents and interfaces in ion-irradiated material volume is a major impediment to attaining a deeper physics-based understanding of the effects of irradiation on the material microstructure and its associated mechanical properties. In this paper, we present a novel indentation approach, which together with the corresponding local structure information obtained from electron back-scattered diffraction (EBSD) and transmission electron microscopy (TEM), allows us to probe nanoscale surface modifications caused by irradiation in solid materials and quantify the resulting changes in its mechanical response.

Among the experimental techniques available at these length scales, nanoindentation, with its high resolution load and depth sensing capabilities, shows the greatest promise due to its non-destructive nature, ease of experimentation (only a polished surface prior to ion irradiation is needed) and versatility [1, 2, 5–7]. In particular, using spherical indenters, our recent work [8–10] has demonstrated the feasibility of transforming the raw load-displacement data into meaningful indentation stress-strain curves. These indentation data analysis methods have successfully captured the local loading and unloading elastic moduli, the local indentation yield strengths, and certain aspects of post-yield strain hardening behavior in various polycrystalline metal samples [11]. More specifically, the use of these indentation stress-strain curves makes it possible to analyze the initial loading segments of spherical indentation before the indentation itself imposes additional local plastic deformation and alters the local microstructure and its properties. Coupling the mechanical data obtained from nanoindentation with the structure information obtained from EBSD has also provided new insights into the local elastic-plastic properties of interest [10, 12, 13]. This has enabled the measurement of the local indentation yield strengths in individual grains of deformed polycrystalline metallic samples [14–16], and across their grain boundaries [17], which in turn can be related to percentage increases in the local slip resistances from their fully annealed conditions. In this paper, these methods are applied to indentations on ion-irradiated metallic materials, and their relative mechanical behavior is compared to the unirradiated state. These questions will be answered by systematically characterizing He, W, and He plus W (He+W) ion irradiated polycrystalline tungsten through spherical nanoindentation of single grains and careful EBSD and TEM of the irradiated layer.

Experimental Details

The ion-radiation experiments were conducted on polycrystalline (grain size range 25–50 µm, see Fig. 1) samples of annealed (at 1500 °C for 3 days) and electro-polished (using a chilled sodium hydroxide solution at 8 V for 1 min [18, 19]) tungsten. The choice of tungsten was motivated due to its potential use as a fusion reactor first wall material and due to the isotropy of its elastic response at the single crystal level.

Figure 1a shows the four regions of a single polycrystalline tungsten sample which were created by masking and subsequent ion beam irradiation. The annealed (electro-polished) condition was characterized prior to ion beam irradiation; however, it also exists in one of the quadrants in the final sample for future characterization. Helium implantation was performed first, followed by W-ion irradiation creating regions with just He and just W irradiation and one region with both He and W (first He and then W, He+W) irradiation. Room temperature helium ion implantation and tungsten ion irradiation were performed on a Danfysik Research Implanter at the Ion Beam Materials Laboratory (IBML) at Los Alamos National Laboratory (LANL). Multiple voltages and fluences were used to create a box-like profile of displacement damage of 0.5 dpa and He concentration of ~1.5 at.% starting from the highest energy: 200 keV at 2.0E16 ions cm^{-2}, 150 keV at 4.0E15 ions cm^{-2}, 100 keV at 8.0E15 ions cm^{-2}, and 50 keV at 7.2E15 ions cm^{-2}. As a result, the He concentration in W was estimated to be about 0.92 atomic% between 150 nm and about 450 nm below the surface using SRIM (Stopping and Range of

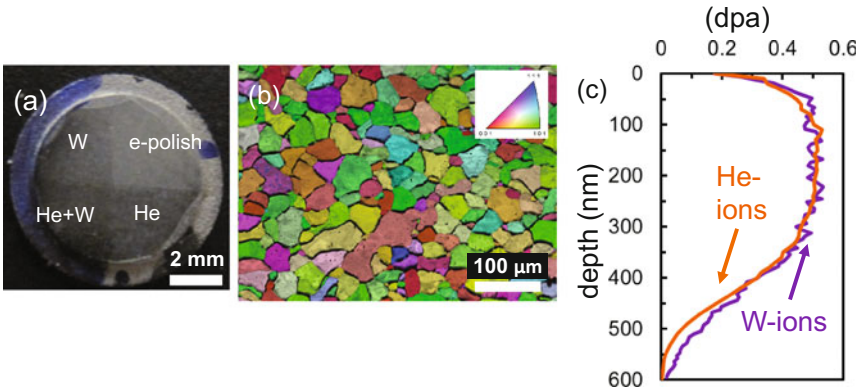

Fig. 1 **a** Four quadrants of a polycrystalline tungsten sample which represent four different sample conditions: unirradiated (electro-polished), He ion irradiated, W ion irradiated, and He followed by W (He+W) ion irradiated. **b** EBSD image quality map with superimposed grain coloring using the inverse pole figure (IPF, shown in inset) scheme. **c** SRIM calculated damage profiles for W-ions and He-ions showing the close match between irradiation experiments

Ions in Matter) Monte Carlo code [20]. The same box-like profile of displacement damage of 0.5 dpa was created for W-irradiation starting from the highest energy: 1.5 meV at 1.3 ion cm^{-2} and 5 meV at 6.2E13 ions cm^{-2}. The SRIM [21] calculated profiles are shown in Fig. 1c.

Nanoindentation was carried out using the Agilent XP® system maintained and operated by the Center for Integrated Nanotechnologies (CINT) at LANL, Los Alamos, NM, USA, and equipped with the Continuous Stiffness Measurement (CSM) option. Three different spherical diamond tips with radii of R_i = 1, 10, and 100 μm, respectively, were used in this study. As discussed later, the different radii of the indenters allow us to explore the influence of indentation zone length scales on the measurements. Multiple indentations (>20) were performed on each sample for each indenter size. The exact indent locations on the sample were verified using a combination of post-indentation EBSD [FEI XL30 Environmental Scanning Electron Microscope (ESEM)], SEM and/or optical micrography. Only indents located in the center of the grains, well away from any interfaces, were considered in the final analysis; indents that landed close to the grain boundaries were ignored.

TEM (FEI Tecnai F30) was used to observe and quantify the defects in the irradiated layer. Figure 2 shows representative TEM micrographs of the dislocation loops and He bubbles in the irradiated layer for He+W. The depth of damage goes to approximately 800 nm; the uniform damaged region is between 200 and 700 nm, and the He bubbles end at a depth of about 500 nm. This is slightly deeper than the SRIM calculated profiles in Fig. 1c. In the uniformly damaged region, the helium bubble density and size determined in the underfocus imaging condition [22] was about 8.5×10^{23} m^{-3} and about 1.1 nm for He implanted tungsten (He) and about

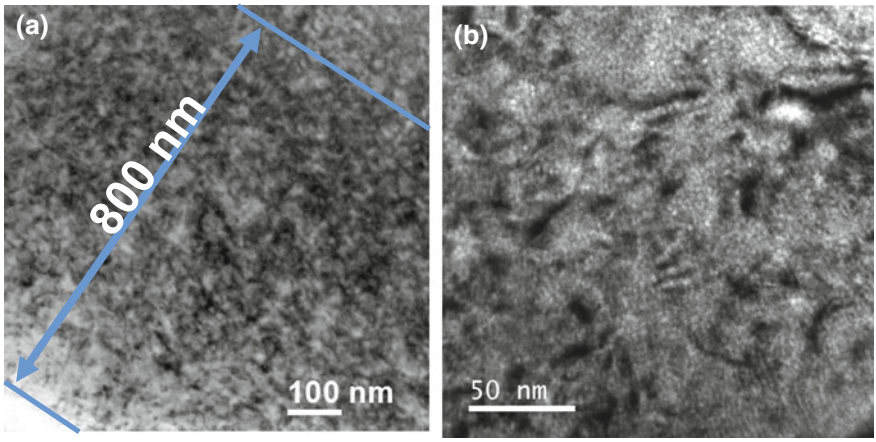

Fig. 2 TEM micrographs on He implanted and W irradiated W. **a** Showing the distribution of dislocation loops across the damaged region. The uniform damaged region is a depth between 200-700 nm. **b** He bubbles are visible in the under focused image. He bubbles end at a depth of ~ 500 nm

9.1×10^{23} m^{-3} and about 1.1 nm for He implanted and W irradiated tungsten (He +W). The average dislocation loop density and size was determined to be about 3×10^{23} m^{-3} and about 3 nm on the He+W region. The dislocation loop measurements are expected to also be representative of the W irradiated tungsten region.

Spherical Indentation Stress-Strain (ISS) Curves

The ability to produce indentation stress-strain curves has generally been more successful with spherical indenters [23, 24], where the relatively smoother stress fields (compared to sharper indenters [25, 26]) allow one to follow the evolution of the mechanical response in the material, from initial elasticity to the initiation of plasticity to post-yield behavior at finite plastic strains. The data analysis protocols used to convert the recorded load-displacement data to indentation stress-strain (ISS) curves can be summarized as a two-step procedure (see Refs. [8, 10] for details). The first step in the analysis process is an accurate estimation of the point of effective initial contact in the given data set, i.e., a clear identification of a zero-point that makes the measurements in the initial elastic loading segment consistent with the predictions of Hertz's theory [27–29]:

$$S = \frac{3P}{2h_e} = \frac{3\left(\tilde{P} - P^*\right)}{2\left(\tilde{h}_e - h^*\right)} \tag{1}$$

where $\tilde{P}$, $\tilde{h}_e$, and S are the measured load signal, the measured displacement signal, and the continuous stiffness measurement (CSM) signal in the initial elastic loading segment from the machine, respectively, and P^* and h^* denote the values of the load and displacement values at the point of effective initial contact. Rearrangement of Eq. (1) reveals that a plot of $\tilde{P} - \frac{2}{3}S\tilde{h}_e$ against S will produce a linear relationship whose slope is equal to $-\frac{2}{3}h^*$ and the y-intercept is equal to P^*. Therefore, a linear regression analysis can then be performed to identify the point of the effective initial contact (P^* and h^*) very accurately.

In the second step, the values of indentation stress and indentation strain can be calculated by recasting Hertz theory for frictionless, elastic, spherical indentation as

$$\begin{gathered} \sigma_{ind} = E_{eff}\varepsilon_{ind}, \sigma_{ind} = \frac{P}{\pi a^2}, \varepsilon_{ind} = \frac{4}{3\pi}\frac{h_e}{a} \approx \frac{h_e}{2.4a}, \\ a = \frac{S}{2E_{eff}}, \frac{1}{E_{eff}} = \frac{1-v_s^2}{E_s} + \frac{1-v_i^2}{E_i}, \frac{1}{R_{eff}} = \frac{1}{R_i} + \frac{1}{R_s} \end{gathered} \tag{2}$$

where σ_{ind} and ε_{ind} are the indentation stress and indentation strain, a is the radius of the contact boundary at the indentation load P, h_e is the elastic indentation depth, S (=dP/dh_e) is the elastic stiffness described earlier, R_{eff} and E_{eff} are the effective

radius and the effective stiffness of the indenter and the specimen system, v and E are the Poisson's ratio and the Young's modulus, and the subscripts s and i refer to the specimen and the indenter, respectively.

The use of spherical indenters also presents an important opportunity to systematically study responses at different material volumetric or length scales by simply varying the indenter radii. This concept has been explored by various research groups including the authors [10, 30] and teams from Drexel University [23, 31], Oak Ridge National Laboratory [32–34] and others [35], and is briefly described below. Since Eqs. 1 and 2 analyze the initial loading segments of the indentation datasets, we can systematically vary the indentation zone sizes at yield (i.e., at the point where the indentation zone is dominated by plastic yielding, Fig. 3a) in the range of 100 nm to >30 μm by using a range of indenter tip radii. This is depicted in the table in Fig. 3d, which shows the approximate indentation depth (h_t) and the corresponding contact radius (a) and the depth of the indentation

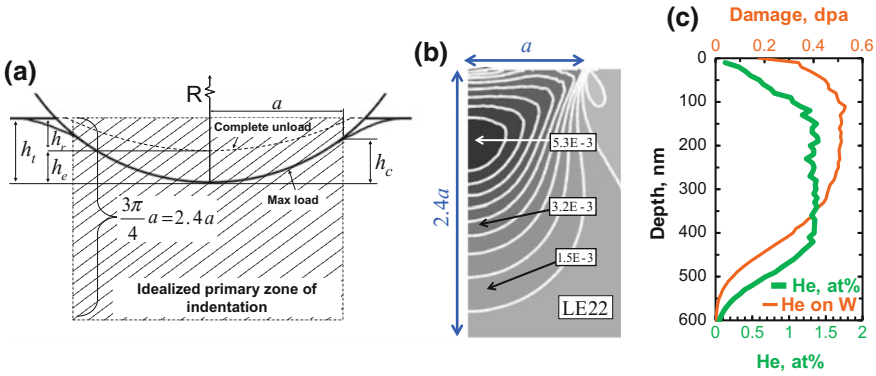

(d)

Indenter radius, R	Indentation depth, h_t	Contact radius, a	Indentation zone ~2.4a
1 μm	~10 nm	60 nm	144 nm
10 μm	~20 nm	250 nm	600 nm
100 μm	~40 nm	1,200 nm	2,880 nm
1000 μm *	>200 nm	12,800 nm	30,720 nm

Fig. 3 **a** Schematic of spherical indentation showing the idealized primary zone of indentation. **b** Logarithmic strain field (along the indentation direction) for a spherical indenter in the indentation zone (~2.4a, where a is the contact radius) close to the indentation yield [36]. Both the contact radius a, and hence the volume probed by indentation, can be controlled with a proper choice of indenter radii. This approach is thus ideally suited for measuring any mechanical changes in the modified material surface layers, such as probing the **c** damage caused by He irradiation on a tungsten sample. **d** Table showing indentation depth (h_t), contact radius (a) and indentation zone size (~2.4a) at yield for W using 4 different indenter radii. *For the 1000 μm radius indenter, the response was all elastic up to h ~200 nm (instrument limit). Figure adapted from Ref [54]

zone (which scales as 2.4*a* [8]) at yield in annealed tungsten for five different indenter radii. This table illustrates the need for a proper choice of the indenter size in order to closely correspond the volume probed by nanoindentation (Fig. 3b [36]) to the depth of He radiation-damaged region (Fig. 3c). The use of three different sized indenter radii (R_i = 1, 10, and 100 μm, see Figs. 1 and 3d) can also reveal some of the salient features of the inherent heterogeneity expected in the sample (in the depth direction). Furthermore, the ability to make a large number of measurements on a given sample surface also has the potential to provide quantitative information on the variance of properties in the irradiated layer.

Results and Discussion

Indentation Stress-Strain Response of Annealed Versus He-Irradiated Tungsten

Figure 4 demonstrates the capability of spherical nanoindentation in reliably characterizing the grain-scale heterogeneities present in metallic materials. Since the length scales in our spherical nanoindentations are much smaller than the typical grain sizes of 25–50 μm in our tungsten sample, the local lattice orientation(s) at the indentation site (measured using EBSD) are expected to strongly influence the elastic-plastic properties of the indents (see Fig. 4a) [14, 37, 38]. In order to successfully study the effects of radiation damage on the indentation behavior, we need to first decouple the effects of orientation from the effects of the increased defect density caused by irradiation.

Figures 4b, c show the comparison of the indentation load-displacement and indentation stress-strain responses respectively for grains whose surface normals were very close (within 6°) to [100] directions. These grains were purposely selected to avoid the need to correct for the effect of the lattice orientation at the indentation site in comparing the different measurements presented in these plots. Of particular interest in the tests on the annealed sample is the occurrence of 'pop-in' events, which are seen as sudden excursions in indentation depth in Fig. 4b and as indentation strain bursts in Fig. 4c. Pop-ins are known to act as a trigger for the onset of plastic deformation [33–35], with the stresses under the indenter reaching extremely high values (approaching the theoretical shear strength of the material) before the pop-in event. Their cause has been generally attributed to the difficulty of activating potent dislocation sources (e.g., Frank-Read sources) [34, 39] in the very small indentation zones (typically much smaller than the length scales associated with dislocation spacing or dislocation cell size) in these experiments [40]. This physical explanation is consistent with the observations that the pop-ins occur most readily in indentation experiments on annealed samples which have very low defect density [41, 42]. Their propensity should decrease with

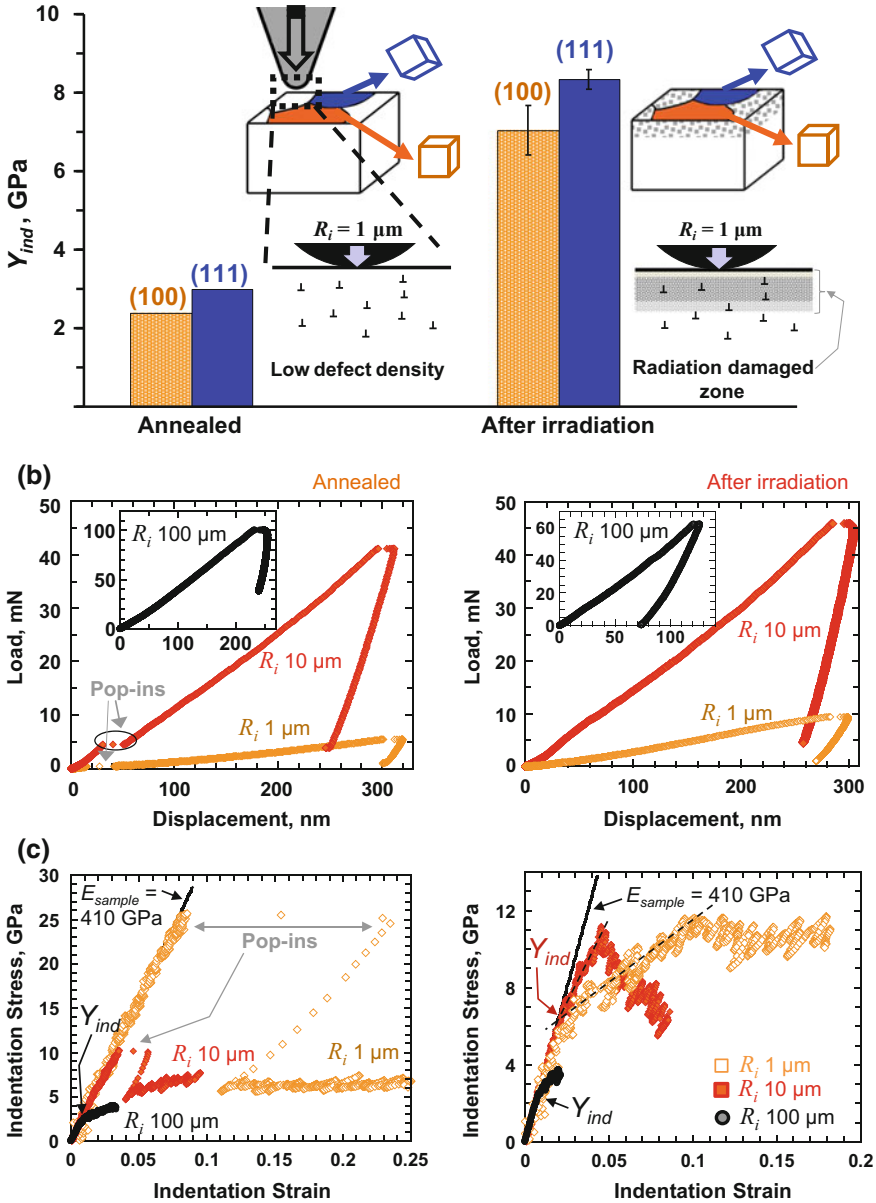

Fig. 4 **a** Causes for the change in Y_{ind}. In annealed electro-polished tungsten, the defect density is low across all grains. Here Y_{ind} varies from one grain to another mainly due to the differences in the activities of the different slip systems in the different grains and their orientation with the indentation direction. Upon ion-irradiation, the metal surface is modified by a damaged layer, which causes a change in its mechanical response as compared to the bulk of the sample. The Y_{ind} in irradiated samples therefore depends on both the grain orientation and the interaction of the indentation zone with the radiation damaged layer at the indentation site Typical **b** load-displacement and **c** indentation stress-strain responses for a near (001) grain in annealed electro-polished tungsten using 3 different indenter sizes of radii 1, 10 and 100 μm before and after He irradiation. Figure adapted from Ref [54]

increasing indentation zone size [10, 33, 43, 44], which increases the likelihood of encountering dislocation sources within the indentation zone. Consistent with this assertion, the very small indenter tip radii of R_i = 1 μm shows the largest indentation strain burst in Fig. 4c, with the burst size decreasing for the larger indenter size of R_i = 10 μm, while the pop-in completely disappears for the largest R_i = 100 μm indenter size [45, 46]. Also, as seen from Fig. 4c, the indentation stress-strain plots with initial pop-ins often exhibit a large discontinuity. This makes it difficult to accurately estimate Y_{ind} from such a plot. It then becomes necessary to use a large indenter radii such as R_i = 100 μm, where pop-ins are absent, to reliably measure Y_{ind} in annealed metals.

The indentation stress-strain curves from the irradiated samples (Fig. 4c) also reveal several novel features. Strikingly, none of the measurements in the irradiated sample (including the measurement with the smallest indenter tip R_i = 1 μm) revealed any pop-ins. A possible explanation could be that the ion-irradiation introduces a large density of defects into the material structure (such as He bubbles and dislocation loops [47], Fig. 2) that can help set up highly potent dislocation sources without any need for pop-ins [48]. Another obvious consequence of these new defects introduced by irradiation is that the Y_{ind} values in the irradiated samples are higher than the corresponding values in the annealed samples. It is also observed that in addition to the higher yield values, the irradiated samples are exhibiting more complex features (e.g., multiple distinct regimes of hardening/softening) compared to the annealed samples.

The differences in indentation stress-strain response before and after irradiation are examined for each indenter size in Figs. 5a–c. Each figure also provides a schematic depiction of the estimated evolving indentation volume at different points of the test [10, 36, 49]. Here the primary zone of indentation deformation is idealized as a cylindrical region of radius a and height 2.4a, where a is the indentation contact radius, with the highest indentation stresses being expected between depths of $\sim a/2$ [28, 36, 49] to a below the indenter (see schematic in Fig. 5a–c). The evolution of a, and by extension that of the primary indentation zone size, is related to the increase in indentation depth and load according to Eq. 2. Additionally, the radiation-damaged region is idealized into four layers labelled A through D (see Table 1) delineating the different zones of radiation damage based on the profile of the imposed He damage concentration. Layer B denotes the region between 150 nm and about 450 nm, where the He concentration in W was estimated to be the highest (about 0.92 at.%). Layers A and C indicate transition regions with strong damage gradients. The bottommost layer D denotes the virgin (undamaged and annealed) material below the radiation affected region.

Figure 5a indicates that the initial indentation yield in the test conducted with the R_i = 1 μm indenter tip occurs at a contact radius of $a \sim 32$ nm. Thus the indentation zone at yield for this test comprises largely of the transition layer A, and the measured Y_{ind} value provides an estimate for the effective indentation yield strength for layer A as 3.7 ± 0.8 and 4.6 ± 0.4 GPa for near-(100) and near-(111) oriented

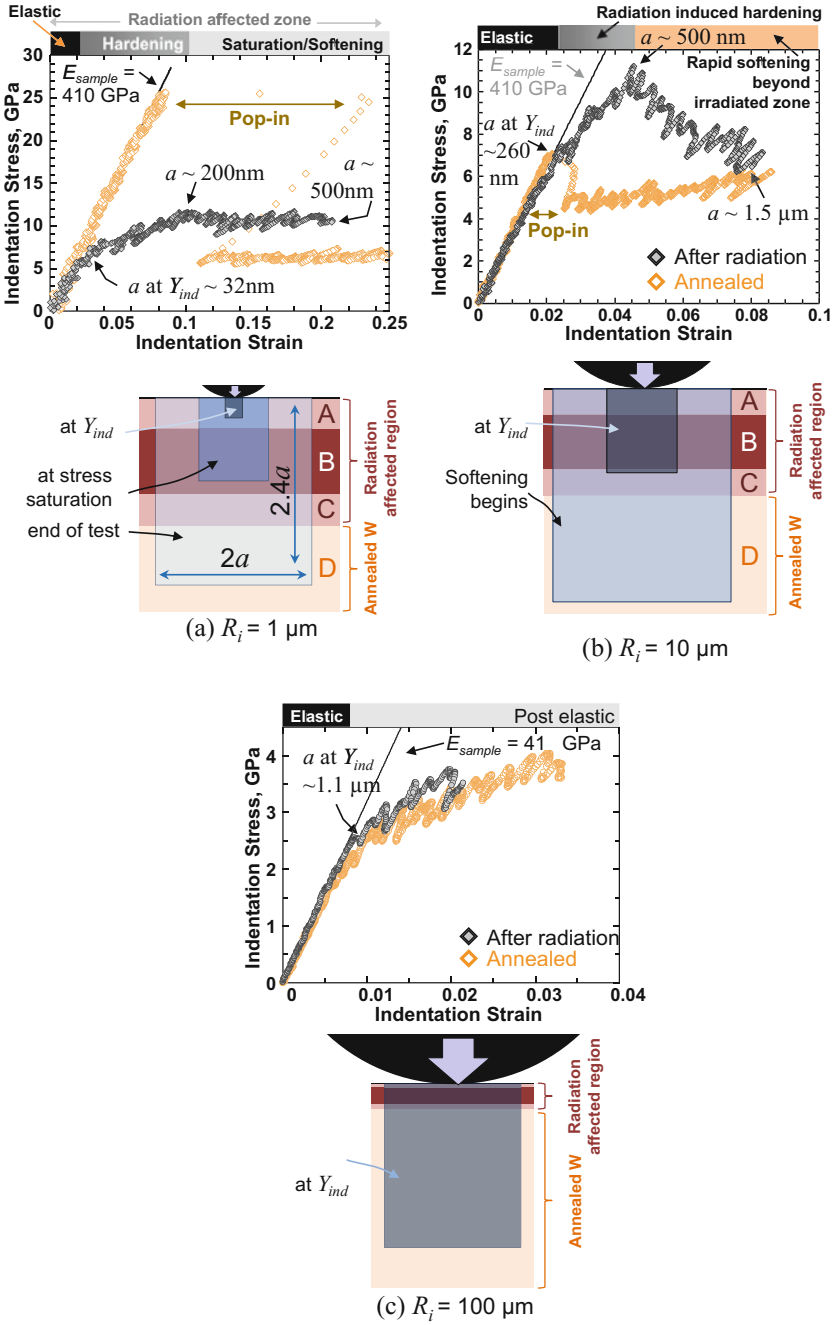

Fig. 5 Comparing the indentation stress-strain responses between annealed (orange curve) and irradiated (black curve) W grains of near (001) orientation for four different indenter tip radii **a** 1 μm, **b** 10 μm and **c** 100 μm (color figure online). Figure adapted from Ref [54]

Table 1 Summary of the results for the indentation measurements performed on the annealed and He irradiated tungsten samples. Adapted from Ref [54]

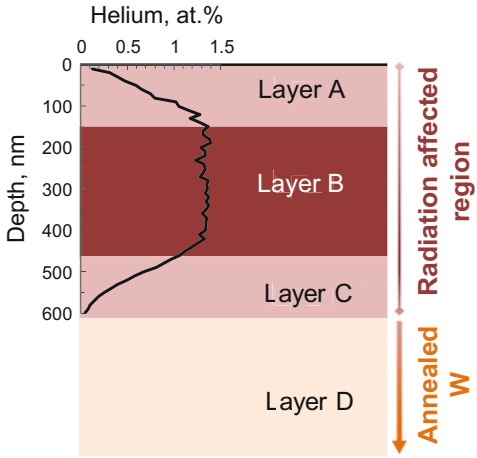

Grain orientation	Layer A Yield stress, GPa	Layer B Yield stress, GPa	Layer D Yield stress, GPa
	Measured as Y_{ind} from R_i=1 µm indenter	Measured as the saturation stress values from R_i=1, µm indenter	Measured as Y_{ind} on annealed W using R_i=100 µm indenter
Near (100)	3.7±0.8	10.1±0.9	2.4±0.4
Near (111)	4.6±0.4	11.3±0.4	3.1±0.3

grains, respectively (see Table 1). With continued loading, the indentation volume increases and gradually includes layer B, which has experienced the highest level of radiation damage. This results in apparent hardening in the indentation stress-strain curve in Fig. 5a between indentation strains of 0.03 and 0.1, i.e., the indentation flow strength appears to increase with indentation strain. It is interesting to note that at about an indentation strain of 0.1 (where $a \sim 200$ nm), the indentation flow strength reaches a saturation value of around 10.5 GPa. There is no further strain hardening detected beyond this point, although the indentation zone is now primarily comprised of the heavily damaged layer B. There is a slight softening in the flow strength towards the end of the test, where the indentation zone now extends to include layers C and D, both of which are expected to be softer than layer B.

The saturation value of indentation flow strength from this test reflects largely the strength of layer B. In other words, if layer A were absent, Y_{ind} from this indentation test would be close to the saturation flow strength value of 10.1 ± 0.9 GPa (average ± standard deviation for near-(100) oriented grains; Table 1). Note that this value is 3.2 times higher than the Y_{ind} of annealed W grains of similar orientation. Large increases in plastic flow strengths are generally accompanied with loss of strain hardening and formation of instabilities such as shear banding [50–52]. We therefore hypothesize that layer B exhibits a high indentation plastic flow strength, but very little real strain hardening under the indenter.

Increasing the indenter size to R_i = 10 μm further confirms the trends described above (Fig. 5b). The initial indentation yield is now higher (Y_{ind} = 6.4 ± 0.5 GPa and 7.4 ± 0.8 GPa for near-(100) and (111) oriented grains respectively), the apparent indentation strain hardening and saturation regimes are shorter, and the subsequent softening regime is even more dominant. Interestingly, the peak indentation flow strength is still around 10 GPa (9.9 ± 0.8 and 9.2 ± 0.5 GPa for the near (100) and near (111) grains respectively), lending support to our earlier hypotheses regarding the mechanical response of layer B. The contact radius at transition between the hardening and softening regimes of the indentation stress-strain response ($a \sim 500$ nm) also matches the depth of the radiation-affected region. As expected, the indentation stress-strain curves from the annealed and the irradiated samples show excellent convergence at larger indentation strains. All of the observations described are a testament to the unique potential of the indentation stress-strain protocols in obtaining meaningful insights into the local mechanical response from exceedingly small volumes.

Increasing the indenter size further to the largest R_i = 100 μm indenter increases the indentation zone to well beyond the radiation damaged region (Fig. 5c). Thus in these measurements, the differences between the annealed and the irradiated samples are very small. This is not surprising since the indentation zone at yield in this test is dominated by layer D.

As described earlier, a major goal of our study was to develop and validate the nanoindentation data analysis methods to rigorously account for the crystal lattice orientation at the indentation site. We suggest that Figs. 4 and 5 and data shown in Table 1 capture this effect reliably and consistently, and could be used in studies on other samples of this material. Table 1 summarizes the values of the indentation yield stress of the various layers in the radiation-affected region of the He-irradiated W sample; the values are compared between near-(100) and near-(111) oriented grains (all grains tested in this work had their surface normals within 6–14° of the [100] and [111] directions). These two particular orientations were chosen since they exhibited the largest differences in the measured Y_{ind} values in prior studies on bcc metals [10, 14, 15]. As discussed earlier, the Y_{ind} values from R_i = 1 μm indenter are expected to be the best representation of the indentation yield strength of layer A. Similarly, the saturation stress for the R_i = 1 μm indenter is thought to represent the indentation yield strength of layer B. R_i = 10 μm indenter also shows similar stress saturation levels. Finally, the indentation yield strength of layer D is

taken as the Y_{ind} values on annealed W using a R_i = 100 μm indenter that does not exhibit pop-ins.

Effect of Ion-Species on the Indentation Stress-Strain Response: Annealed, He, W Versus He+W Irradiation

Based on the results from Section "Indentation Stress-Strain Response of Annealed Versus He-Irradiated Tungsten" above, an exhaustive investigation of multiple grain orientations in tungsten, and their effects upon irradiation using different ion species (He, W and He+W), was conducted [53]. Since Figs. 2, 4 and 5 show that the irradiated layer is limited to the first 800 nm of the sample, R_i = 1–10 μm radii indenters were chosen to determine the indentation properties.

Figure 6 shows representative indentation stress-strain curves for R_i = 1 and 10 μm radius indenters for all four regions (annealed, He, W, and He+W ion-irradiated tungsten) for grains close to the (100) crystal direction. The y-axis of Fig. 6a is purposely chosen to focus on the irradiated condition and not the pop-ins which have been cutoff in this plot. We note multiple similar observations between Fig. 6 and Section "Indentation Stress-Strain Response of Annealed Versus He-Irradiated Tungsten", such as the lack of pop-ins in the indentation response of the irradiated samples, and the different responses between the R_i = 1 and 10 μm radius indenters. An important new observation from Fig. 6 is that the He implanted tungsten exhibits higher plastic flow strengths compared to W irradiated tungsten. This conclusion is reached by comparing the saturation indentation stresses in the R_i = 1 μm indenter test and the indentation yield strengths in the R_i = 10 μm indenter test. This is despite the fact that these two regions exhibited the same SRIM calculated displacement damage. This observation suggests that He bubbles play a more dominant role in the mechanical response compared to just dislocation loops. This is also evident in the region of the tungsten sample where He implantation was performed first followed by W irradiation (He+W). Indentation tests in this region show the same response as the He implanted (He) region, also implying that the relative role of loops on the plastic flow stress is significantly lower compared to the He bubbles.

Orientation Effects on the Indentation Stress-Strain Response of the Irradiated Material

One of the advantages of spherical nanoindentation protocols is that many grain orientations can be tested in a high-throughput manner. Figure 7 shows the grain orientations that were tested for each irradiated region for two indenter sizes

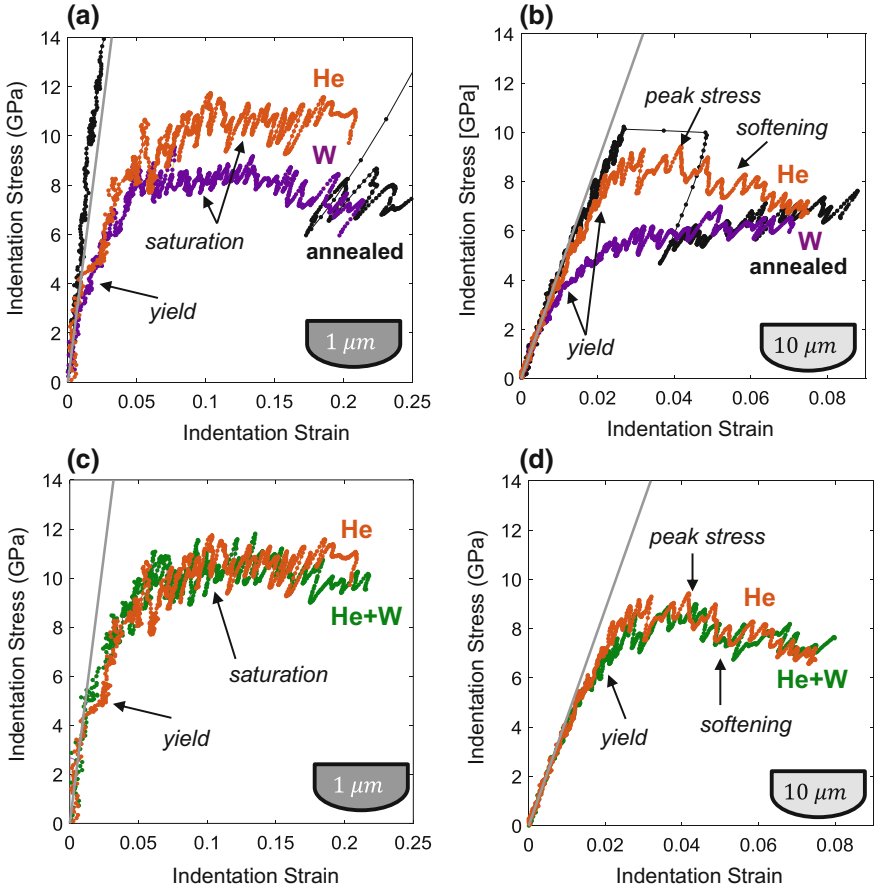

Fig. 6 Representative indentation stress-strain curves for two different indenter sizes and four different conditions: **a** 1 μm radius indenter for annealed unirradiated, He-ion irradiated, and W-ion irradiated. **b** 10 μm radius indenter for annealed unirradiated, He-ion irradiated, and W-ion irradiated. **c** 1 μm radius indenter for He-ion irradiated and He+W ions irradiated. **d** 10 μm radius indenter for He-ion irradiated and He+W ions irradiated. All orientations are near (100) direction so as to remove any orientation effects from the comparisons. The modulus line represents the indentation modulus using a Young's modulus of 405 GPa and a Poisson's ratio of 0.28 (i.e., E_{ind} = 405/(1 − 〖0.28〗 ^2) = 439 GPa). Figure adapted from Ref [53]

(R_i = 1 and 10 μm radii) that were near the three poles [i.e., (100), (101), and (111)] in the inverse pole figure. The average strength values (1 μm saturation stress and 10 μm 0.2% yield strength) are also shown in Fig. 7. Similar to trends showed earlier in Table 1, the orientation trend for the indentation yield strength $\left(Y_{ind}^{(100)} < Y_{ind}^{(111)}\right)$ present in the unirradiated material is no longer apparent in the

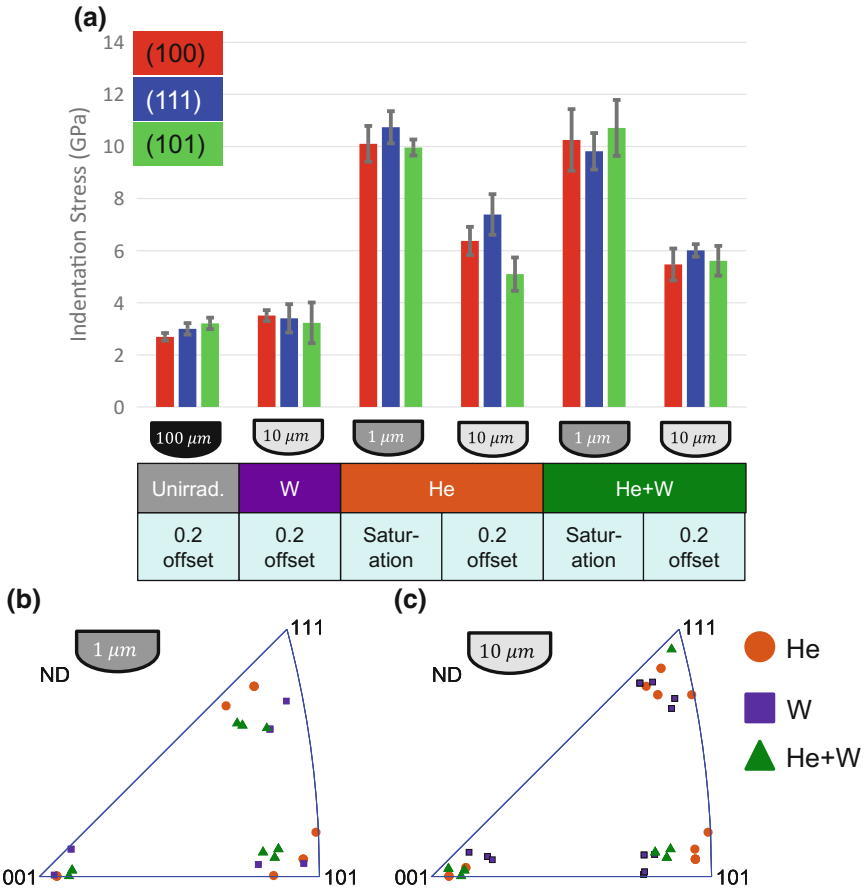

Fig. 7 **a** Average indentation strength measurements for different indenter sizes, definitions of strength, conditions, and grain orientations. **b** The grain orientations tested for R_i = 1 μm indenter and **c** R_i = 10 μm indenter. Figure adapted from Ref [53]

irradiated material. The irradiated material appears to behave more plastically isotropic than the unirradiated material. There is a level of uncertainty in this observation as seen by the large error bars in most cases. These error bars relate both to the large spread of orientations seen in the IPF maps (Fig. 7b, c) as well as the inherent scatter of the nanoindentation measurements. In other words, some orientation trend could exist that would be unresolvable because of the variance in the measurements. Additional work is clearly required to study the grain orientation effects in the irradiated samples.

Conclusion

In summary, the measurements show our first attempts at utilizing spherical indentation stress-strain curves to investigate the changes in the mechanical response of tungsten with ion-irradiation induced surface damages. These methods are cost-effective in extracting huge amounts of reliable and reproducible information from very small nanometer sample volumes. By simply varying the indenter size, this technique can be used to provide new insights into the mechanical response of the irradiated layers in these samples, and correlate those effects with the local material structure obtained from EBSD. As such, the ideas presented in this communication are applicable to all polycrystalline material systems (including metals and ceramics) with a modified surface layer. They can also be extended to a broad range of complex material systems where the local structure information is obtained by other materials characterization techniques (e.g., Raman-spectroscopy maps on bone [55], back-scattered electron images).

Acknowledgements The authors acknowledge funding from Department of Energy, Nuclear Engineering Enabling Technologies (DOE-NEET)—Reactor Materials program # DE-FOA-0000799, and University of California Office of the President (UCOP) under Award Number 12—LR237801 for this work. This work was performed, in part, at the Center for Integrated Nanotechnologies, an Office of Science User Facility operated for the U.S. Department of Energy (DOE) Office of Science. Los Alamos National Laboratory, an affirmative action equal opportunity employer, is operated by Los Alamos National Security, LLC, for the National Nuclear Security Administration of the U.S. Department of Energy under contract DE-AC52-06NA25396. SP gratefully acknowledges funding from the Los Alamos National Laboratory Director's Postdoctoral Fellowship and University of Nevada, Reno start-up faculty funds for this work.

References

1. J.T. Busby, M.C. Hash, G.S. Was, The relationship between hardness and yield stress in irradiated austenitic and ferritic steels. J. Nucl. Mater. **336**(2–3), 267–278 (2005)
2. P. Hosemann, J.G. Swadener, D. Kiener, G.S. Was, S.A. Maloy, N. Li, An exploratory study to determine applicability of nano-hardness and micro-compression measurements for yield stress estimation. J. Nucl. Mater. **375**(1), 135–143 (2008)
3. D. Kiener, P. Hosemann, S.A. Maloy, A.M. Minor, In situ nanocompression testing of irradiated copper. Nat. Mater. **10**(8), 608–613 (2011)
4. N. Li, N.A. Mara, Y.Q. Wang, M. Nastasi, A. Misra, Compressive flow behavior of Cu thin films and Cu/Nb multilayers containing nanometer-scale helium bubbles. Scr. Mater. **64**(10), 974–977 (2011)
5. A.C. Fischer-Cripps, *Nanoindentation*, 2nd edn. (Springer, 2004)
6. P. Hosemann, D. Kiener, Y. Wang, S.A. Maloy, Issues to consider using nano indentation on shallow ion beam irradiated materials. J. Nucl. Mater. **425**(1–3), 136–139 (2012)
7. P. Hosemann, C. Vieh, R.R. Greco, S. Kabra, J.A. Valdez, M.J. Cappiello, S.A. Maloy, Nanoindentation on ion irradiated steels. J. Nucl. Mater. **389**(2), 239–247 (2009)
8. S.R. Kalidindi, S. Pathak, Determination of the effective zero-point and the extraction of spherical nanoindentation stress–strain curves. Acta Mater. **56**(14), 3523–3532 (2008)

9. S. Pathak, J. Shaffer, S.R. Kalidindi, Determination of an effective zero-point and extraction of indentation stress-strain curves without the continuous stiffness measurement signal. Scr. Mater. **60**(6), 439–442 (2009)
10. S. Pathak, S.R. Kalidindi, Spherical nanoindentation stress–strain curves. Mater. Sci. Eng. R: Rep. **91**, 1–36 (2015)
11. S.J. Vachhani, R.D. Doherty, S.R. Kalidindi, Effect of the continuous stiffness measurement on the mechanical properties extracted using spherical nanoindentation. Acta Mater. **61**(10), 3744–3751 (2013)
12. D. Raabe, N. Zaafarani, R.N. Singh, F. Roters, S. Zaefferer, Three-dimensional investigation of the texture and microstructure below a nanoindent in a Cu single crystal using 3D EBSD and crystal plasticity finite element simulations. Acta Mater. **54**(7), 1863–1876 (2006)
13. M. Rester, C. Motz, R. Pippan, The deformation-induced zone below large and shallow nanoindentations: a comparative study using EBSD and TEM. Philos. Mag. Lett. **88**(12), 879–887 (2008)
14. S. Pathak, D. Stojakovic, S.R. Kalidindi, Measurement of the local mechanical properties in polycrystalline samples using spherical nano-indentation and orientation imaging microscopy. Acta Mater. **57**(10), 3020–3028 (2009)
15. S.J. Vachhani, S.R. Kalidindi, Grain-scale measurement of slip resistances in aluminum polycrystals using spherical nanoindentation. Acta Mater. **90**, 27–36 (2015)
16. J.S. Weaver, M.W. Priddy, D.L. McDowell, S.R. Kalidindi, On capturing the grain-scale elastic and plastic anisotropy of alpha-Ti with spherical nanoindentation and electron back-scattered diffraction. Acta Mater. **117**, 23–34 (2016)
17. S. Pathak, J. Michler, K. Wasmer, S.R. Kalidindi, Studying grain boundary regions in polycrystalline materials using spherical nano-indentation and orientation imaging microscopy. J. Mater. Sci. **47**(2), 815–823 (2012)
18. G. Petzow, *Metallographic Etching: Techniques for Metallotraphy, Ceramography, Plastography*, 2nd edn. ASM International (1999)
19. *ASM Handbook: Volume 9: Metallography And Microstructures*. ASM International. ISBN: 978-0-87170-706-2 (2004)
20. J. Ziegler, J. Biersack, The stopping and range of ions in matter, in: *Treatise on Heavy-Ion Science*, ed. by D.A. Bromley (Springer, USA, 1985), pp. 93–129
21. J.F. Ziegler, J.P. Biersack, *SRIM Program* (IBM Corp., Yorktown, NY, 2008)
22. M.L. Jenkins, M.A. Kirk, *Characterisation of Radiation Damage by Transmission Electron Microscopy*. CRC Press (2000)
23. S. Basu, A. Moseson, M.W. Barsoum, On the determination of spherical nanoindentation stress–strain curves. J. Mater. Res. **21**(10), 2628–2637 (2006)
24. J.S. Field, M.V. Swain, Determining the mechanical properties of small volumes of material from submicrometer spherical indentations. J. Mater. Res. **10**(1), 101–112 (1995)
25. J.L. Bucaille, S. Stauss, E. Felder, J. Michler, Determination of plastic properties of metals by instrumented indentation using different sharp indenters. Acta Mater. **51**(6), 1663–1678 (2003)
26. A.E. Giannakopoulos, S. Suresh, Determination of elastoplastic properties by instrumented sharp indentation. Scr. Mater. **40**(10), 1191–1198 (1999)
27. H. Hertz, *Miscellaneous Papers* (MacMillan and Co., Ltd., New York, 1896)
28. K.L. Johnson, *Contact Mechanics* (Cambridge University Press, Cambridge, 1987)
29. I.N. Sneddon, The relation between load and penetration in the axisymmetric Boussinesq problem for a punch of arbitrary profile. Int. J. Eng. Sci. **3**, 47–56 (1965)
30. J.S. Weaver, A. Khosravani, A. Castillo, S.R. Kalidindi, High throughput exploration of process-property linkages in Al-6061 using instrumented spherical microindentation and microstructurally graded samples. Integrating Mater. Manufact. Innov. **5**(1), 1–20 (2016)
31. M.W. Barsoum, M. Radovic, T. Zhen, P. Finkel, S.R. Kalidindi, Dynamic elastic hysteretic solids and dislocations, Phys. Rev. Lett. **94**(8), 085501-1 (2005)

32. H. Bei, Y.F. Gao, S. Shim, E.P. George, G.M. Pharr, Strength differences arising from homogeneous versus heterogeneous dislocation nucleation. Phys. Rev. B. **77**(6) (2008)
33. J.R. Morris, H. Bei, G.M. Pharr, E.P. George, Size effects and stochastic behavior of nanoindentation pop in. Phys. Rev. Lett. **106**(16) (2011)
34. S. Shim, H. Bei, E.P. George, G.M. Pharr, A different type of indentation size effect. Scr. Mater. **59**(10), 1095–1098 (2008)
35. C.A. Schuh, Nanoindentation studies of materials. Mater. Today **9**(5), 32–40 (2006)
36. B.R. Donohue, A. Ambrus, S.R. Kalidindi, Critical evaluation of the indentation data analyses methods for the extraction of isotropic uniaxial mechanical properties using finite element models. Acta Mater. **60**(9), 3943–3952 (2012)
37. J.J. Vlassak, W.D. Nix, Indentation modulus of elastically anisotropic half spaces. Philos. Mag. A (Physics of Condensed Matter, Defects and Mechanical Properties) **67**(5), 1045–1056 (1993)
38. J.J. Vlassak, W.D. Nix, Measuring the elastic properties of anisotropic materials by means of indentation experiments. J. Mech. Phys. Solids **42**(8), 1223–1245 (1994)
39. S.A. Syed Asif, J.B. Pethica, Nanoindentation creep of single-crystal tungsten and gallium arsenide. Philos. Mag. A. (Physics of Condensed Matter: Structure, Defects and Mechanical Properties) **76**(6), 1105–1118 (1997)
40. Y. Gao, H. Bei, Strength statistics of single crystals and metallic glasses under small stressed volumes. Prog. Mater Sci. **82**, 118–150 (2016)
41. Z. Wang, H. Bei, E.P. George, G.M. Pharr, Influences of surface preparation on nanoindentation pop-in in single-crystal Mo. Scr. Mater. **65**(6), 469–472 (2011)
42. S. Pathak, D. Stojakovic, R. Doherty, S.R. Kalidindi, Importance of surface preparation on the nano-indentation stress-strain curves measured in metals. J. Mater. Res. Focus Issue Indentation Methods Adv. Mater Res. **24**(3), 1142–1155 (2009)
43. S. Pathak, J.L. Riesterer, S.R. Kalidindi, J. Michler, Understanding pop-ins in spherical nanoindentation. Appl. Phys. Lett. **105**(16), 161913 (2014)
44. S. Shim, H. Bei, M.K. Miller, G.M. Pharr, E.P. George, Effects of focused ion beam milling on the compressive behavior of directionally solidified micropillars and the nanoindentation response of an electropolished surface. Acta Mater. **57**(2), 503–510 (2009)
45. T.A. Michalske, J.E. Houston, Dislocation nucleation at nano-scale mechanical contacts. Acta Mater. **46**(2), 391–396 (1998)
46. S. Suresh, T.G. Nieh, B.W. Choi, Nano-indentation of copper thin films on silicon substrates. Scr. Mater. **41**(9), 951–957 (1999)
47. M. Victoria, N. Baluc, C. Bailat, Y. Dai, M.I. Luppo, R. Schaublin, B.N. Singh, The microstructure and associated tensile properties of irradiated fcc and bcc metals. J. Nucl. Mater. **276**, 114–122 (2000)
48. M. Miyamoto, D. Nishijima, M.J. Baldwin, R.P. Doerner, Y. Ueda, K. Yasunaga, N. Yoshida, K. Ono, Microscopic damage of tungsten exposed to deuterium-helium mixture plasma in PISCES and its impacts on retention property. J. Nucl. Mater. **415**(1), S657–S660 (2011)
49. D.K. Patel, H.F. Al-Harbi, S.R. Kalidindi, Extracting single-crystal elastic constants from polycrystalline samples using spherical nanoindentation and orientation measurements. Acta Mater. **79**, 108–116 (2014)
50. T. Diaz de la Rubia, H.M. Zbib, T.A. Khraishi, B.D. Wirth, M. Victoria, M.J. Caturla, Multiscale modelling of plastic flow localization in irradiated materials. Nature **406**(6798), 871–874 (2000)
51. N.A. Mara, D. Bhattacharyya, J.P. Hirth, P. Dickerson, A. Misra, Mechanism for shear banding in nanolayered composites. Appl. Phys. Lett. **97**(2), 021909 (2010)
52. A. Patra, D.L. McDowell, Crystal plasticity-based constitutive modelling of irradiated bcc structures. Philos. Mag. **92**(7), 861–887 (2012)
53. J.S. Weaver, C. Sun, Y. Wang, S.R. Kalidindi, N.A. Mara, S. Pathak, Comparing irradiation induced damage in He, W and He+W ion irradiated tungsten using spherical nanoindentation (2017 submitted)

54. S. Pathak, J.S. Weaver, S.R. Kalidindi, Y. Wang, R. Doerner, N. Mara, Probing nanoscale damage gradients with spherical nanoindentation. Scientific Reports. **7**, 11918 (2017). doi:10.1038/s41598-017-12071-6
55. S. Pathak, S.J. Vachhani, K.J. Jepsen, H.M. Goldman, S.R. Kalidindi, Assessment of lamellar level properties in mouse bone utilizing a novel spherical nanoindentation data analysis method. J. Mech. Behav. Biomed. Mater (2012). doi:10.1016/j.jmbbm.2012.03.018